Topologically Protected Supercoupling in Cavity-Integrated Photonic Structure for Terahertz Communication

Tushar Shah
Department of Electronics and Electrical Engineering
Indian Institute of Technology, Guwahati
Assam, India
tushar.shah@iitg.ac.in

Dibaskar Biswas
Department of Electronics and Electrical Engineering
Indian Institute of Technology, Guwahati
Assam, India
dibaskar.biswas@iitg.ac.in

Lokesh Sharma
Department of Electronics and Electrical Engineering
Indian Institute of Technology, Guwahati
Assam, India
sharma.123lokesh@gmail.com

Sourodipto Das
Department of Electronics and Electrical Engineering
Indian Institute of Technology, Guwahati
Assam, India
d.sourodipto@iitg.ac.in

Ashish Kumar Chowdhary
Department of Electronics and Communication Engineering
Indian Institute of Technology, Roorkee
Uttarakhand, India
ashish.chowdhary@ece.iitr.ac.in

Debabrata Sikdar
Department of Electronics and Electrical Engineering
Indian Institute of Technology, Guwahati
Assam, India
deb.sikdar@iitg.ac.in

Abstract— **Topological photonics uses the two inequivalent band extrema (K and K′) as binary labels to steer light along topological domain wall interfaces with improved robustness and directionality—this is the core concept behind topological photonics. Terahertz integrated photonic cavities are an important component for many applications including sensing, signal processing and communication systems. However, efficient excitation of such cavities usually requires very small coupling gaps, which limits layout flexibility and increases fabrication complexity. Since the valley edge modes have long evanescent tails and a vortex-like energy flow, the cavity can be excited efficiently when the coupling gap is less than or equal to half of the lattice spacing (a). This paper presents a super-coupled cavity made from a high resistive silicon (HR-Si) with circular air hole valley photonic crystal (VPC) platform. The structure is operating within the 310–340 GHz bandgap. A triangular cavity is created at the junction of straight topological edge waveguides. It demonstrates that it is possible to maintain strong coupling to the cavity and high isolation between the input/output ports, while maintaining good transport properties of the topological interface. This super-coupled cavity structure provides a versatile platform for realizing compact THz resonators, topological lasers, and sensors. The results also demonstrate that valley photonic crystals provide basis for developing on-chip coupling with robust cavity operation in future terahertz photonic integrated circuits.**

Keywords— Topological photonics, Valley photonic crystals, Cavity, Photonic Integrated Circuits, Super-coupling, edge states.

I. INTRODUCTION

Terahertz (THz) photonic integrated circuits have gained significant interest due to their potential applications in high speed wireless transmission, spectroscopy, sensing and miniaturized signal processing systems [1], [2]. In the majority of THz photonic integrated circuits, on chip resonant cavities are one of the primary components that enable localized optical fields, enhance light-matter interactions, and allow frequency selective operation [3]. The design requirements for many photonic cavities rely upon the evanescent coupling across deeply sub-wavelength gap spacings [4]. These stringent layout restrictions, increased fabrication sensitivities, and limited scalability in large scale circuit integration all represent major drawbacks associated with conventional photonic cavities.

Photonic integrated circuits (PICs) have emerged as a core platform for realizing high-speed, low-power, and compact on-chip systems, enabling a wide range of applications including optical signal processing, data communication, quantum computing, and sensing technologies [1], [2], [4], [5]. As the scale and functional complexity of PICs continue to grow, increasing on-chip integration density while maintaining efficient interconnection between photonic components has become a critical design challenge. In particular, precise control over waveguide and cavity coupling plays a decisive role in determining the performance, scalability, and robustness of integrated photonic architectures.

Conventional coupling schemes in PICs predominantly rely on evanescent field interactions between closely spaced waveguides or between waveguides and resonators [6]. Due to the rapid spatial decay of evanescent fields, effective coupling is typically limited to sub-wavelength separation distances, making the coupling strength highly sensitive to fabrication tolerances and alignment errors [7], [8] . Similar limitations arise in the excitation of on-chip photonic cavities, where achieving critical coupling requires extremely small and accurately controlled coupling gaps [9], [10]. These constraints hinder the realization of flexible, long-reach coupling architectures and restrict layout freedom in dense photonic integration.

Several approaches have been explored to extend coupling distances by modifying the modal field distribution, including low-index-contrast waveguides fabricated using femtosecond laser direct writing techniques [11], [12] , as well as geometry-

engineered photonic crystal waveguides [13], [14]. Although such methods enable partial control over mode tail length, they often suffer from increased radiation loss, momentum mismatch, fabrication complexity, and limited compatibility with standard CMOS fabrication processes[14], [15]. Sub-wavelength structures such as gratings and optical metamaterials have also been proposed to tailor coupling behaviour [16], [17], [18]; however, achieving compact, low-loss, and broadband long-range coupling remains a significant challenge.

Recent advances in topological photonics provide a promising solution to these limitations. In particular, valley photonic crystal (VPC) platforms enable the formation of topologically protected edge modes with tunable mode tails and momentum-conserved vortex energy flow [19], [20], [21]. This phenomenon, known as photonic topological super-coupling, allows efficient waveguide and cavity coupling over distances ranging from sub-wavelength to multiple wavelengths while maintaining low loss and strong robustness against fabrication imperfections. Such capabilities introduce a new degree of freedom for realizing compact, alignment-tolerant, and high-performance integrated photonic systems [22].

Inspired by the above described benefits, this work presents a super-coupled cavity design using a circular hole valley photonic crystal operating within the 310–340 GHz (0.31-0.34 THz) frequency range. A Triangular Cavity is created at the intersection point of two straight topological edge waveguides, which enables efficient excitation of the cavity via valley-protected interface modes. Unlike standard evanescent coupling methods, strong coupling to the cavity is maintained even when the waveguide-cavity separation approaches half of the lattice constant. Simultaneously, high isolation between input and output channels are preserved, while maintaining robust transport along the topological interface.

These results demonstrate that the proposed structure represents a compact and flexible platform for realizing long range on-chip coupling in the THz regime. Furthermore, the results highlight the potential of VPC architectures for developing miniaturized resonators, sensors and topological light sources with reduced spacing constraints and improved robustness, paving the way towards practical THz photonic integrated circuits.

II. Design of VPC Unit Cell and Numerical Modelling

A. VPC Unit-Cell Design

The VPC unit cell employed in this work is based on silicon with high resistive ($\rho > 10k\Omega$-cm) slab patterned with circular air holes as depicted in Fig. 1(a). To induce non-trivial topological properties, inversion symmetry of the unit cell is intentionally broken by introducing two inequivalent air holes with radii $r_1 = \frac{1.3a}{3\sqrt{3}}$ and $r_2 = \frac{0.7a}{3\sqrt{3}}$ for VPC-1 and for VPC-2, r_1 and r_2 are interchanged. The degree of inversion symmetry is breaking through a radius perturbation factor defined as $\Delta r = |r_1 - r_2| = \frac{0.6a}{3\sqrt{3}}$, where a represents the lattice constant of photonic structure. When $r_1 = r_2$, the unit cell preserves inversion symmetry. Introducing unequal radii breaks this symmetry and changes the valley-dependent properties of the structure. Interchanging r_1 and r_2 produces two VPCs with opposite valley characteristics while maintaining the same geometrical periodicity.

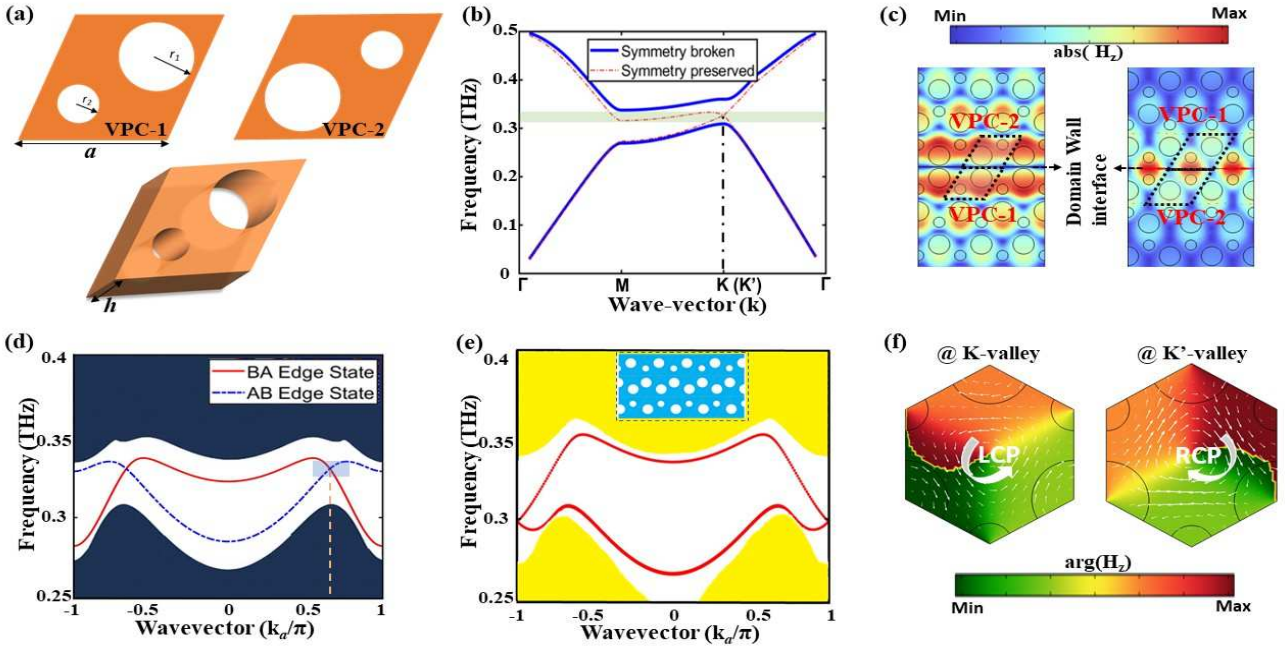

Fig.1: (a) Schematic representation of two VPCs unit cell and its 3D view, (b) Band-diagram for symmetric ($\Delta r = 0$) and asymmetric ($\Delta r = \frac{0.6a}{3\sqrt{3}}$) VPCs. The shaded portion represents the photonic bandgap regions, (c) Field distribution plot with zigzag domain wall interfaces: AB-type (left) and BA-type (right), (d) Dispersion (Edge-state) plot with different zigzag edge interfaces, (e) Dispersion plot with bearded interface, (inset showing bearded interfaces of VPCs) and (f) Phase maps showing vortex-like energy flow and topological phase transition at K and K'-valley point.

B. Numerical Modelling and Boundary Conditions

The unit-cell and band-structure calculations were performed using the eigenfrequency solver in COMSOL Multiphysics®. Bloch–Floquet periodic boundary conditions were applied to the opposite boundaries of the unit cell. The silicon was modelled using an effective refractive index ($n = 3$), while the air holes were assigned ($n = 1$). The wave vector was varied along the (Γ-M-K- Γ) path of the first Brillouin zone. A refined mesh was used near the silicon–air interfaces to accurately resolve the electromagnetic fields and eigenfrequencies.

C. Calculation of the Bulk Band Diagram

For the inversion-symmetric case ($r_1 = r_2$), the calculated band diagram exhibits degenerate Dirac cones at the (K) and (K') points. When $r_1 \neq r_2$, i.e.; inversion symmetry is broken, which lifts the degeneracy of the Dirac cones at the K and K′ points of the Brillouin zone and it leads to the opening of a photonic bandgap of approximately 0.31-0.34 THz as shown in Fig. 1(b). This simulation was performed using COMSOL Multiphysics® software. Since, a photonic bandgap is opened without breaking time-reversal symmetry, which enables valley-dependent modal behavior that is essential for realizing topological edge transport.

III. Analysis of Topological Edge States and Phase Transition

To investigate topological edge state modes, a supercell structure is made by combining two VPC unit cells with mirrored sublattice configurations. Here, VPC-1 is also called as 'Type-B' and VPC-2 as 'Type-A' cell. The arrangement of VPC-1 and VPC-2 forms a domain wall interface (shown in Fig. 1(c)), where the edge modes are confined at this interface of VPCs. This leads to the emergence of topologically protected valley locked edge states, also known as valley kink states. In this study, three interface configurations are examined, namely the AB-type zigzag interface, the BA-type zigzag interface, and the bearded interface. Periodic boundary conditions are applied along the propagation direction, while scattering boundary conditions are employed along the transverse direction to minimize unwanted boundary reflections.

The edge-state dispersion characteristics are obtained by solving the eigenmodes of the supercell configuration. These edge states are basically dispersion diagrams as shown in Fig. 1(d), (e). These resulting dispersion diagrams exhibit gap-crossing modes located within the edge bandgap region. These modes are strongly confined to the domain wall and display directional propagation behaviour associated with valley locking. Among the considered interface types, the bearded interface shows enhanced mode isolation and reduced coupling to bulk states, indicating improved confinement and superior edge transport performance.

To further validate the topological nature of the guided modes, electromagnetic field distributions and phase profiles are analysed at representative frequencies inside the bandgap. The surface field plots show strong energy localization along the interface region (Fig. 1(c)) and the corresponding phase transition maps exhibit vortex-like circulation patterns (depicted in Fig. 1(f)), which are characteristic signatures of valley-polarized energy flow. These observations confirm that the proposed VPC structure supports robust edge transport with suppressed backscattering, making it suitable for terahertz topological waveguiding and cavity-based applications.

IV. Calculation of Berry Phase, and Berry Curvature

In the context of topological photonics, Berry phase and curvature play a crucial role in understanding how wave propagation is influenced by topological properties, specifically within the 2D-photonic crystal structure. In valley-type topological photonics structure, by breaking spatial inversion symmetry in a hexagonal lattice, the Dirac degeneracy at K and K′ points lift to open a photonic gap. This gap introduces opposite Berry curvatures, which acts as an effective magnetic field in the momentum space that leads to topological valley transport. When a wave continuously passing along a closed path, its state continuously varying in momentum space of a periodic system. In this momentum space, the wavevector ($\boldsymbol{k}$) also changing within closed loop due to periodic nature of lattice. So, it accumulates a phase, i.e. geometrical phase, named as Berry phase. In a periodic photonic crystal, the eigenvalue problem is given by [23]:

$$H(\boldsymbol{k})\phi_n(\boldsymbol{k}) = \lambda_n(\boldsymbol{k})\phi_n(\boldsymbol{k})$$

where $\phi_n(\boldsymbol{k})$ and $\lambda_n(\boldsymbol{k})$ are the normalized eigen wavefunction of Hamiltonian $H(\boldsymbol{k})$ and eigen energy, respectively at each $\boldsymbol{k}$ for the n^{th} band [24].

For the analysis of Berry phase, it is necessary to acquire the phase contributions from each small change obtained in the wave function. The phase difference between two ϕ_n states that are very closely spaced, separated by small change in momentum ($d\boldsymbol{k}$) can be expressed through their inner product as [23]:

$$\langle \phi_n(\boldsymbol{k}) | \phi_n(\boldsymbol{k} + d\boldsymbol{k}) \rangle$$

For a periodic system like a hexagonal lattice, the Berry phase $\gamma(k)$ is calculated along a closed path in momentum space. As the momentum vector k changes, the wavefunction gains a phase, which is Berry phase or geometric phase; given as [23], [24]:

$$\gamma(k) = \int_{\Gamma} \boldsymbol{A}(\boldsymbol{k}) \cdot d\boldsymbol{k}$$

where Γ represents the loop in momentum space that the wavevector $\boldsymbol{k}$ traces and $\boldsymbol{A}(\boldsymbol{k})$ is the Berry connection, represents the interaction between the momentum $\boldsymbol{k}$ and the wavefunctions. In a 2D photonic crystal lattice, the Berry connection can be explicitly computed by the following relations [23], [24]:

$$\boldsymbol{A}(\boldsymbol{k}) = i\langle \phi_n(\boldsymbol{k}) \mid \nabla_{\boldsymbol{k}} \mid \phi_n(\boldsymbol{k}) \rangle\rangle$$

The Berry curvature, or berry flux $\Omega(\boldsymbol{k})$, which measures the "twist" in the wavefunction, is the curl of the Berry connection [23], [24]:

$$\Omega(\boldsymbol{k}) = \nabla_{\boldsymbol{k}} \times A(\boldsymbol{k})$$

and the Berry curvature in two dimensions is given by [23]:

$$\Omega(k_x, k_y) = \frac{\partial A_y(k_x, k_y)}{\partial k_x} - \frac{\partial A_x(k_x, k_y)}{\partial k_y}$$

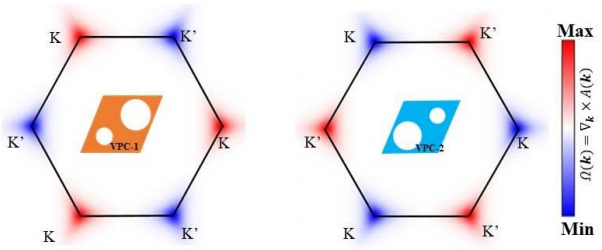

Fig. 2: Berry-curvature distribution in momentum space for the two VPC configurations (VPC-1 and VPC-2) within the first Brillouin zone.

This curvature plays a role in determining the Chern number, a topological invariant that helps identify edge states in the system. The Chern number is related to the Berry curvature over the entire Brillouin zone (BZ) and can be calculated as[24]:

$$C_n = \frac{1}{2\pi}\int_{BZ} \Omega(k_x, k_y).d^2\boldsymbol{k}$$

Therefore, using all above expressions, we have calculated the Berry curvature numerically as shown in Fig. 2. In this fig., strong and opposite Berry-curvature localization is observed at K and K′ points of the Brillouin zone, indicating valley-dependent topological phase transition.

V. Full Structure Design with Topological Cavity

The full structure design of waveguide along with topological cavity was build and simulated using the commercially available software CST Microwave Studio Suite®. The 3D structure created by combining arrays of VPCs (VPC-1 and VPC-2), made up of high resistive silicon with resistivity (ρ > 10kΩcm), thickness (*h*) = 200 µm, dielectric constant of 11.7, with lattice periodicity i.e. lattice constant (*a*) = 242.5 µm. By arranging the VPC-1 and VPC-2 in systematic manner, the domain wall interface is created. This interface is useful to guide THz wave along this interface path. We have designed a straight waveguide with a topological triangular cavity as shown in Fig. 3(a). there are three ports used in this design where port-1 is input port and other two ports (port-2 and port-3) are output ports for THz signal. In the triangular cavity, one side domain wall path of this cavity made with bearded type interface to support slow light effects for enhancing the light matter interaction at this interface.

VI. Results and Discussion

A. Supercoupling in Topological Cavities

The simulation of the topological cavity structure reveal significant insights into the super-coupling effect, particularly in the transmission spectra and electromagnetic field distributions. The Fig. 3(b) shows the transmission response of the designed structure with clear noticeable dip in S_{21}, highlights the super-coupling phenomenon. This super-coupling effect occurs at the frequency of edge state crossing points of type AB and type BA interface i.e. 328.6 GHz (depicted in Fig. 1(d)). In this region, energy is efficiently transferred between straight waveguide and the cavity. The sharp resonance occurrence is a critical component for

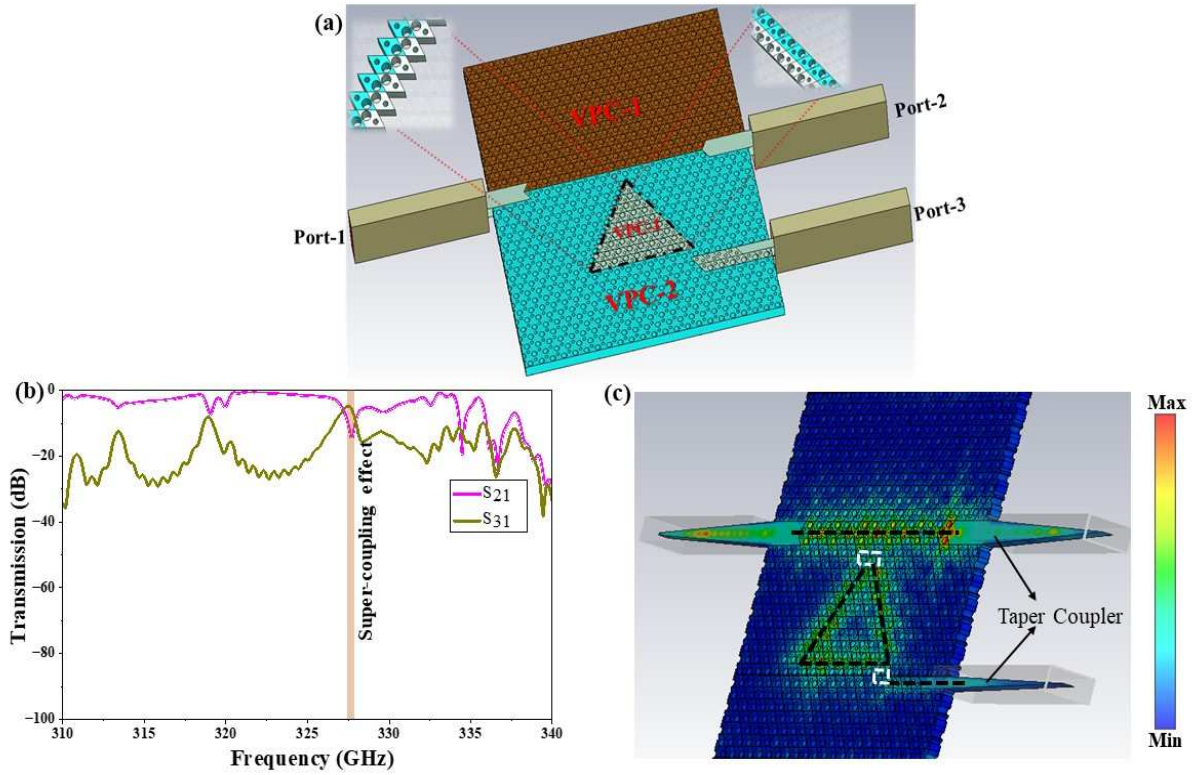

Fig. 3: (a) Schematic diagram of full structure of topological waveguide along with topological cavity (marked as black dotted line) with three ports. The inset shows bearded interface on one side (left) and zigzag interfaces on other two sides (right & bottom) of triangular cavity (b) Transmission spectra at port-2 (S_{21}) and port-3 (S_{31}). The area highlighted shows super-coupling effect region, and (c) Field distribution plot along the domain wall paths. The white regions marked here is super-coupling areas.

improving light matter interaction, which boost the performance of topological integrated photonic circuits for terahertz sensing and lasing for terahertz communication.

B. Electromagnetic Field Distribution

The effectiveness of this topological structure is further confirmed by the field distribution plot, where the taper coupler ensures the optimal coupling between the cavity and waveguide. In Fig. 3(c), the electromagnetic field distribution within the topological cavity, showing the enhancement of field intensity near the cavity interface. The heatmap clearly hotspotted the areas where the electromagnetic field is confined, particularly along the edges within domain wall interfaces and cavity. In the highlighted regions, the topologically protected edge states are localized. This field distribution is crucial for understanding the role of the cavity geometry in guiding the wave and enhancing transmission at resonant frequencies.

VII. CONCLUSION

In this work, we have shown the potential of topologically protected super-coupling in cavity-integrated photonic devices for terahertz communication. Particularly at the resonant frequencies, where super-coupling greatly enhances light-matter interaction, our models clearly demonstrate an improvement in the transmission characteristics. Effective energy transfer between the waveguide and cavity is shown by the prominent resonance seen in the transmission spectra (S_{21} and S_{31}), particularly at the super-coupling region around 328.6 GHz. Furthermore, a slow light effect results from the significant confinement of electromagnetic waves along the topologically protected edges, which is highlighted by the field distribution inside the cavity. This slow light behavior is essential for improving light-matter interaction, which is fundamental for potential applications in terahertz sensing, lasing in communication, and other photonic devices. These findings provide new opportunities for the development of terahertz devices with improved light-matter interactions, potentially improving performance for next generation communication technologies. Further optimization in the geometry of the cavity could lead to stronger coupling and broaden the operational bandwidth, making it a promising solution for future high-performance integrated photonic circuits.

ACKNOWLEDGMENT

This work was supported by Senior Research Fellowship provided by Ministry of Education (MoE), Government of India, and TTDF/6G/328 Project Grant provided by Department of Telecommunication (DoT), Government of India.

REFERENCES

[1] J. Wang *et al.*, "On-chip silicon photonic signaling and processing: a review," Oct. 15, 2018, *Elsevier B.V.* doi: 10.1016/j.scib.2018.05.038.

[2] J. E. Bowers *et al.*, "Recent advances in silicon photonic integrated circuits," in *Next-Generation Optical Communication: Components, Sub-Systems, and Systems V*, SPIE, Feb. 2016, p. 977402. doi: 10.1117/12.2221943.

[3] S. Vincent *et al.*, "Design of tunable metasurfaces for ultra-broadband absorption in terahertz imaging applications," *J. Phys. D Appl. Phys.*, vol. 58, no. 33, Aug. 2025, doi: 10.1088/1361-6463/adf85d.

[4] D. Pérez-López *et al.*, "Large-scale photonic processors and their applications," *NPJ Nanophotonics*, vol. 2, no. 1, Dec. 2025, doi: 10.1038/s44310-025-00075-4.

[5] S. Daudlin *et al.*, "Three-dimensional photonic integration for ultra-low-energy, high-bandwidth interchip data links," *Nat. Photonics*, vol. 19, no. 5, pp. 502–509, May 2025, doi: 10.1038/s41566-025-01633-0.

[6] A. Kumari *et al.*, "Ultra-sensitive wide-angle and polarization-independent terahertz metamaterial absorbers for early detection of basal cell carcinoma," *Phys. Scr.*, vol. 100, no. 10, Oct. 2025, doi: 10.1088/1402-4896/ae0f64.

[7] N. Acharyya *et al.*, "Multiple Critical Couplings and Sensing in a Microresonator-Waveguide System," *Phys. Rev. Appl.*, vol. 8, no. 3, Sep. 2017, doi: 10.1103/PhysRevApplied.8.034029.

[8] A. Prinzen *et al.*, "Fabrication tolerances of SOI based directional couplers and ring resonators," *Opt. Express*, vol. 21, no. 14, p. 17212, Jul. 2013, doi: 10.1364/oe.21.017212.

[9] E. Waks *et al.*, "Coupled mode theory for photonic crystal cavity-waveguide interaction," 2005.

[10] A. Faraon *et al.*, "Efficient photonic crystal cavity-waveguide couplers," *Appl. Phys. Lett.*, vol. 90, no. 7, Feb. 2007, doi: 10.1063/1.2472534.

[11] A. Szameit *et al.*, "Control of directional evanescent coupling in fs laser written waveguides," 2007.

[12] Y. C. Jia *et al.*, "Femtosecond laser direct writing of flexibly configured waveguide geometries in optical crystals: Fabrication and application," *Opto-Electronic Advances*, vol. 3, no. 10, pp. 1–12, 2020, doi: 10.29026/oea.2020.190042.

[13] P. E. Barclay *et al.*, "Design of photonic crystal waveguides for evanescent coupling to optical fiber tapers and integration with high-Q cavities," 2003. doi: 10.1364/OA_License_v1#VOR.

[14] H. S. Dutta *et al.*, "Coupling light in photonic crystal waveguides: A review," Jul. 01, 2016, *Elsevier B.V.* doi: 10.1016/j.photonics.2016.04.001.

[15] Y. Ooka *et al.*, "CMOS compatible high-Q photonic crystal nanocavity fabricated with photolithography on silicon photonic platform," *Sci. Rep.*, vol. 5, Jun. 2015, doi: 10.1038/srep11312.

[16] W. Zhou *et al.*, "Subwavelength engineering in silicon photonic devices," *IEEE Journal of Selected Topics in Quantum Electronics*, vol. 25, no. 3, May 2019, doi: 10.1109/JSTQE.2019.2899757.

[17] Y. Meng *et al.*, "Optical meta-waveguides for integrated photonics and beyond," Dec. 01, 2021, *Springer Nature*. doi: 10.1038/s41377-021-00655-x.

[18] J. M. Luque-González *et al.*, "A review of silicon subwavelength gratings: Building break-through devices with anisotropic metamaterials," Sep. 01, 2021, *De Gruyter Open Ltd*. doi: 10.1515/nanoph-2021-0110.

[19] R. Jia *et al.*, "Photonic Supercoupling in Silicon Topological Waveguides," *Advanced Materials*, vol. 37, no. 6, Feb. 2025, doi: 10.1002/adma.202415083.

[20] R. Jia *et al.*, "On-Chip Active Supercoupled Topological Cavity," *Advanced Materials*, vol. 37, no. 24, Jun. 2025, doi: 10.1002/adma.202419261.

[21] R. Jia *et al.*, "Valley-conserved topological integrated antenna for 100-Gbps THz 6G wireless," 2023. [Online]. Available: https://www.science.org

[22] D. Biswas *et al.*, "Actively tunable wideband terahertz topological power splitter with customizable splitting ratio," *J. Phys. D Appl. Phys.*, vol. 59, no. 8, p. 085107, Feb. 2026, doi: 10.1088/1361-6463/ae45ba.

[23] D. Bisharat *et al.*, "Photonic Topological Insulators: A Beginner's Introduction [Electromagnetic Perspectives]," *IEEE Antennas Propag. Mag.*, vol. 63, no. 3, pp. 112–124, Jun. 2021, doi: 10.1109/MAP.2021.3069276.

[24] K. Goudarzi *et al.*, "Calculation of the Berry curvature and Chern number of topological photonic crystals," *Journal of the Korean Physical Society*, vol. 81, no. 5, pp. 386–390, Sep. 2022, doi: 10.1007/s40042-022-00530-x.